frontiers | Frontiers in Physics

TYPE Original Research
PUBLISHED 10 March 2025
DOI 10.3389/fphy.2025.1548966

OPEN ACCESS

EDITED BY
Francisco Vega Reyes,
University of Extremadura, Spain

REVIEWED BY
Edtson Emilio Herrera Valencia,
National Autonomous University of Mexico, Mexico
Alvaro Rodriguez Rivas,
University of Seville, Spain

*CORRESPONDENCE
Kuniyasu Saitoh,
k.saitoh@cc.kyoto-su.ac.jp

RECEIVED 20 December 2024
ACCEPTED 20 February 2025
PUBLISHED 10 March 2025

CITATION
Saitoh K (2025) Shear strength, avalanches, and structures of soft cohesive particles under shear.
Front. Phys. 13:1548966.
doi: 10.3389/fphy.2025.1548966

Shear strength, avalanches, and structures of soft cohesive particles under shear

Kuniyasu Saitoh*

Department of Physics, Faculty of Science, Kyoto Sangyo University, Kyoto, Japan

The physics of granular materials, including rheology and jamming, is strongly influenced by cohesive forces between the constituent grains. Despite significant progress in understanding the mechanical properties of granular materials, it remains unresolved how the range and strength of cohesive interactions influence mechanical failure or avalanches. In this study, we use molecular dynamics simulations to investigate simple shear flows of soft cohesive particles. The particles are coated with thin sticky layers, and both the range and strength of cohesive interactions are determined by the layer thickness. We examine shear strength, force chains, particle displacements, and avalanches, and find that these quantities change drastically even when the thickness of the sticky layers is only 1% of the particle diameter. We also analyze avalanche statistics and find that the avalanche size, maximum stress drop rate, and dimensionless avalanche duration are related by scaling laws. Remarkably, the scaling exponents of the scaling laws are independent of the layer thickness but differ from the predictions of mean-field theory. Furthermore, the power-law exponents for the avalanche size distribution and the distribution of the dimensionless avalanche duration are universal but do not agree with mean-field predictions. We confirm that the exponents estimated from numerical data are mutually consistent. In addition, we show that particle displacements at mechanical failure tend to be localized when the cohesive forces are sufficiently strong.

KEYWORDS

granular materials, avalanche, plasticity, cohesive interaction, molecular dynamics

1 Introduction

Mechanics of granular materials is of great importance in technologies for sands, foods, and pharmaceutical products [1, 2]. Except for well controlled laboratory experiments, granular materials in nature are usually "wet" with water [3]. Wet granular materials consist of sticky particles, where interactions between them are cohesive due to liquid bridges formed at their contact points [4]. It is known that cohesive interactions strongly influence mechanical properties of granular materials [5]; the critical angle and the angle of repose for landslides significantly increase with the increase of amount of water (or layer thickness), the shear strength (stress) increases with the increase of *suction*[1], the critical acceleration for fluidization of vibrated granular beds increases with the increase of liquid content, and segregation is suppressed and hysteresis is enhanced by the cohesive interactions.

1 The suction is defined as the pressure difference between a liquid bridge and air.

Furthermore, it has been suggested that, if granular materials are wet, jamming occurs at low packing fractions and inhomogeneity, i.e., localization of particle motions, is more pronounced [3].

One of the fundamental problems of granular matter is mechanical failure or *avalanche* which can be related to sediment disasters and earthquakes [6–8]. In seismology, the frequency of earthquake magnitude is explained by the celebrated Gutenberg-Richter (GR) law [7, 8]. As the GR law, statistical properties of mechanical failure are of central interest to physicists, where statistics of avalanches have been studied in the context of self-organized criticality (SOC) [9] or non-equilibrium phase transitions [10]. The SOC indicated by power-law distributions of avalanche (cluster) sizes is realized by a cascade of local failure. Associated the cascade of local mechanical failure with the *depinning transition* [11], power-law scaling of avalanche size distribution was suggested by a mean-field (MF) theory [12–15]. The MF theory also predicts several scaling laws for slip avalanches and its predictions (including the power-law scaling of avalanche size distribution) have been validated by many experiments of, e.g., granular materials under shear [16–19], compressed nano-crystals [20, 21], bulk metallic glasses [22–25], and light flux from a star [26]. Therefore, the statistics of avalanches have been said to be universal, in the sense that scaling exponents for the avalanche size distribution and other quantities do not depend on any details of materials on a microscopic scale.

In addition to experiments, the statistics of avalanches in granular materials have widely been studied by numerical simulations. Nevertheless, the avalanche size distributions extracted from numerical data quantitatively differ from the MF prediction. For example, the power-law exponents for avalanche size distribution found in molecular dynamics (MD) simulations of foams [27] and athermal quasi-static (AQS) simulations of amorphous solids [28–32] are much smaller than the MF prediction. Moreover, different from the MF theory, a mesoscopic elasto-plastic (EP) model was developed on the basis of *yielding transition* [33]. The EP model includes a "quadrupolar" elastic propagator in its governing equation and predicts a smaller power-law exponent for avalanche size distribution [34]. Thus, there still exist discrepancies in the theories, experiments, and simulations, and researchers have carefully examined the roles of system size [35], strain rate [36–39], particle inertia [40–43], friction [44, 45], and particle shapes [46, 47] in the statistics of avalanches. However, much less attention has been paid to the influence of cohesive interactions, which are crucial to real granular materials.

In this paper, we carry out numerical simulations of soft cohesive particles under shear. The main aim of our simulations is to clarify effects of cohesive forces (between the particles) on the statistics of avalanches. We employ a cohesive contact model which has been used for the studies of rheology [48–52] and jamming [53–55] of two-dimensional cohesive particles. We assume that our system is in a *pendular state*, i.e., liquid bridges are formed at contact points so that cohesive interactions are pairwise [4]. We show that not only the statistics of avalanches but also mechanical responses, force-chains, and particle rearrangements are affected by the cohesive interactions even if their range is only 1% of particle diameter. In the following, we explain our numerical methods (Section 2), show our results (Section 3), and discuss our findings (Section 4). All the details of our simulations and supporting data are summarized in Supplementary Material (SM).

2 Numerical methods

In this section, we introduce our numerical methods. We study simple shear deformations of soft cohesive particles in two dimensions by MD simulations. Employing MD simulations, we can easily control the range and strength of cohesive forces, and directly calculate stress from numerical data. Thus, in contrast to the EP model [33] and other continuum models [56], the advantage of our method is that the effect of cohesive interactions on avalanches can be unambiguously examined. In the following, we explain our numerical model of soft cohesive particles (Section 2.1) and show how the system is prepared and applied simple shear deformations (Section 2.2).

2.1 Cohesive contact model

In ordinary MD simulations of soft frictionless particles [57], a contact force between the particles, i and j, is modeled as $\boldsymbol{f}_{ij} = f_{ij}^{\mathrm{e}}\boldsymbol{n}_{ij} - \eta\boldsymbol{v}_{ij}$. Here, $\boldsymbol{n}_{ij} = \left(\boldsymbol{r}_i - \boldsymbol{r}_j\right)/r_{ij}$ with the inter-particle distance, $r_{ij} = \left|\boldsymbol{r}_i - \boldsymbol{r}_j\right|$, is the unit vector parallel to the normal direction, where $\boldsymbol{r}_i$ ($\boldsymbol{r}_j$) is the position of the particle i (j). In the contact force, $-\eta\boldsymbol{v}_{ij}$ represents viscous interaction, where η is the viscosity coefficient and $\boldsymbol{v}_{ij} = \dot{\boldsymbol{r}}_i - \dot{\boldsymbol{r}}_j$ is the relative velocity between the particles in contact. The magnitude of elastic force f_{ij}^{e} is given by a linear spring as $f_{ij}^{\mathrm{e}} = k\delta_{ij}$, where k is the stiffness and $\delta_{ij} = d_{ij} - r_{ij} > 0$ with the sum of particle radii, $d_{ij} \equiv R_i + R_j$, represents an overlap between the particles.

In contrast, soft cohesive particles are modeled by coating the soft frictionless particles with sticky layers [48–55]. It is assumed that every particle is covered by a thin sticky layer with the thickness $2aR_i$, where a is introduced as a small dimensionless parameter. The interaction between the particles is attractive if two layers are overlapped. In our MD simulations, we model the contact force as $\boldsymbol{f}_{ij} = f_{ij}^{\mathrm{c}}\boldsymbol{n}_{ij} - \eta\boldsymbol{v}_{ij}$, where the magnitude of cohesive force f_{ij}^{c} scaled by kd_{ij} is given by

$$\frac{f_{ij}^{\mathrm{c}}}{kd_{ij}} = \begin{cases} -\hat{\delta}_{ij} - 2a & \left(-2a < \hat{\delta}_{ij} < -a\right) \\ \hat{\delta}_{ij} & \left(-a < \hat{\delta}_{ij}\right) \end{cases}. \tag{1}$$

Here, $\hat{\delta}_{ij} \equiv \delta_{ij}/d_{ij}$ is the scaled overlap [58]. As shown in Figure 1, the interaction is attractive, i.e., $f_{ij}^{\mathrm{c}} < 0$, if the scaled overlap is in the range, $-2a < \hat{\delta}_{ij} < 0$, whereas it is repulsive, i.e., $f_{ij}^{\mathrm{c}} > 0$, if the scaled overlap is positive, $\hat{\delta}_{ij} > 0$. Note that a potential energy for the cohesive interaction, Eq. (1), is a continuous and smooth function of the inter-particle distance r_{ij} (see SM). In addition, the viscous force $-\eta\boldsymbol{v}_{ij}$ acts on the particle if $-2a < \hat{\delta}_{ij}$, where either two layers or particles are overlapped.

2.2 Simple shear deformations

We prepare our system as a 50:50 binary mixture of N soft cohesive particles, where two kinds of particles have the same mass

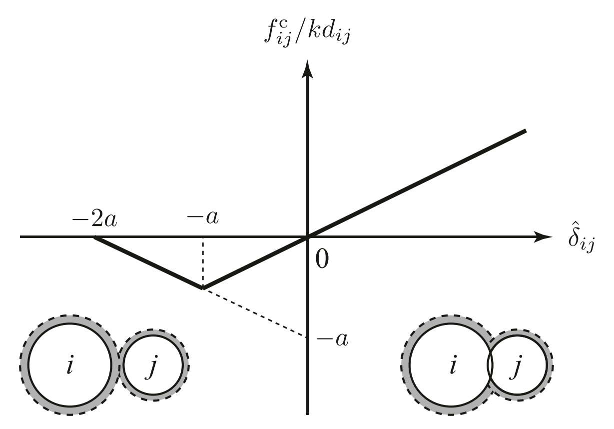

FIGURE 1
A schematic picture of the scaled magnitude of cohesive force, Equation 1. If the scaled overlap is positive, $\hat{\delta}_{ij} > 0$, two particles (circles) are overlapped, where the interaction is repulsive, i.e., $f^c_{ij} > 0$. If $-2a < \hat{\delta}_{ij} < 0$, the particles are not overlapped, while two sticky layers (shaded regions) are overlapped and the interaction is attractive, i.e., $f^c_{ij} < 0$. If $\hat{\delta}_{ij} < -2a$, no force acts on the particles, i.e., $f^c_{ij} = 0$.

m and different diameters, d_S and $d_L = 1.4d_S$ [59]. We randomly distribute the particles in a $L \times L$ square periodic box such that packing fraction of the particles is given by $\phi = \pi\left(d_S^2 + d_L^2\right)N/8L^2$. Note that the area of sticky layers is not included in ϕ.

To apply simple shear deformations to the system, we employ the Lees-Edwards boundary condition. In each time step, we replace every particle position, $\boldsymbol{r}_i = (x_i, y_i)$, with $(x_i + \Delta\gamma y_i, y_i)$ $(i = 1, \ldots, N)$ and numerically integrate equations of motion, $m\ddot{\boldsymbol{r}}_i = \sum_{j(\neq i)} \boldsymbol{f}_{ij}$. We use $\Delta\gamma = 10^{-7}$ for the strain increment and $\Delta t = 10^{-1} t_0$ for the time increment, where $t_0 \equiv \eta/k$ is a unit of time [60]. The shear rate is defined as $\dot{\gamma} \equiv \Delta\gamma/\Delta t = 10^{-6} t_0^{-1}$ which we fix throughout the simulation.

In the following, we analyze the system in a steady state, where the amount of shear strain γ exceeds unity, i.e., $\gamma > 1$. In a steady state, the energy injected by shear is dissipated by the viscous forces between the particles, $-\eta\boldsymbol{v}_{ij}$. Therefore, the injection of energy and the energy dissipation are balanced such that any observables, e.g., shear stress, are steady. We vary the number of particles (the system size) N and the packing fraction ϕ in the ranges, $512 \le N \le 131072$ and $0.8 \le \phi \le 0.9$, respectively. Furthermore, we scale every time and length by the units, t_0 and $d_0 = (d_L + d_S)/2$, respectively.

3 Results

In this section, we show our numerical results of soft cohesive particles under shear. First, we examine how the cohesive forces alter force-chain networks (Section 3.1) and affect macroscopic mechanical responses (Section 3.2). Second, we analyze the effect of cohesive interactions on time-averaged stress (Section 3.3). Third, we introduce slip avalanches and examine their dependence on the cohesive interactions (Section 3.4). Then, we study how scaling laws (Section 3.5) and statistics of avalanches (Section 3.6) are changed by the cohesive forces. In addition, we show that localized non-affine displacements are characteristic of avalanches in soft cohesive particles (Section 3.7).

3.1 Force-chain networks

The structure of force-chain networks of soft cohesive particles under shear is strongly influenced by the range of cohesive interactions. Figure 2A displays snapshots of force-chain networks, where the systems are sheared (as indicated by the horizontal arrows in the top panel) and have reached steady states. In this figure, a small system size, $N = 512$, is used for visualization, where the dimensionless parameter for the cohesive forces is given by $a = 10^{-6}$ (top) and 10^{-2} (bottom). The packing fraction of the particles is $\phi = 0.82$ which is much smaller than the *jamming transition density*, $\phi_J \simeq 0.8433$, for soft frictionless particles in two dimensions [59]. If the thickness of sticky layers is sufficiently small (Figure 2A top), the particles are homogeneously distributed and the force-chain network (solid lines) is weak and homogeneous. However, increasing a, we observe that the particles aggregate with each other—as the "gelation" [61, 62] — and strong force-chains are transmitted through the system (Figure 2A bottom). In other words, if the range of cohesive interactions is sufficient, the system is partially jammed and jammed regions percolate through the system. Figures 2B, C show *non-affine displacements* of the particles and changes of force-chain networks, respectively, which will be discussed in later (Section 3.7).

3.2 Macroscopic mechanical responses

We quantify mechanical responses of soft cohesive particles to simple shear deformations by shear stress. We calculate stress tensor of the system according to the Born-Huang expression [63],

$$\sigma_{\alpha\beta} = -\frac{1}{L^2}\sum_{i<j} f_{ij} r_{ij} n_{ij\alpha} n_{ij\beta} \quad (\alpha, \beta = x, y). \tag{2}$$

Here, $f_{ij} = |\boldsymbol{f}_{ij}|$ is the magnitude of contact force between the particles, i and j, and each component of the normal unit vector is written as $\boldsymbol{n}_{ij} = \left(n_{ijx}, n_{ijy}\right)$. The shear stress is defined as the average of off-diagonal elements, $\sigma = \left(\sigma_{xy} + \sigma_{yx}\right)/2$. Figure 3A displays *stress-strain curves*, i.e., σ vs γ, where the shear stress is scaled by the stiffness k. Increasing the strain γ from zero, we observe that σ increases from zero and becomes steady when γ exceeds unity. The steady state shear stress tends to be large if the thickness of sticky layer or a increases (as indicated by the vertical arrow in Figure 3A). In SM, we show our results of granular temperature, pressure, and macroscopic friction coefficient [64–68] as functions of γ. We find that, though the granular temperature and pressure p exhibit similar dependence on the layer thickness a, the macroscopic friction coefficient defined as $\mu = \sigma/p$ is less sensitive to a.

The influence of cohesive force f^c_{ij} on the shear stress σ is intuitively understood as follows. As shown in Figure 3B, we consider typical configurations of the particles under shear. In general, the system under simple shear deformations is compressed along −45 degrees diagonal and decompressed along 45° diagonal [69]. If the particles, i and j, are aligned in the compressive direction

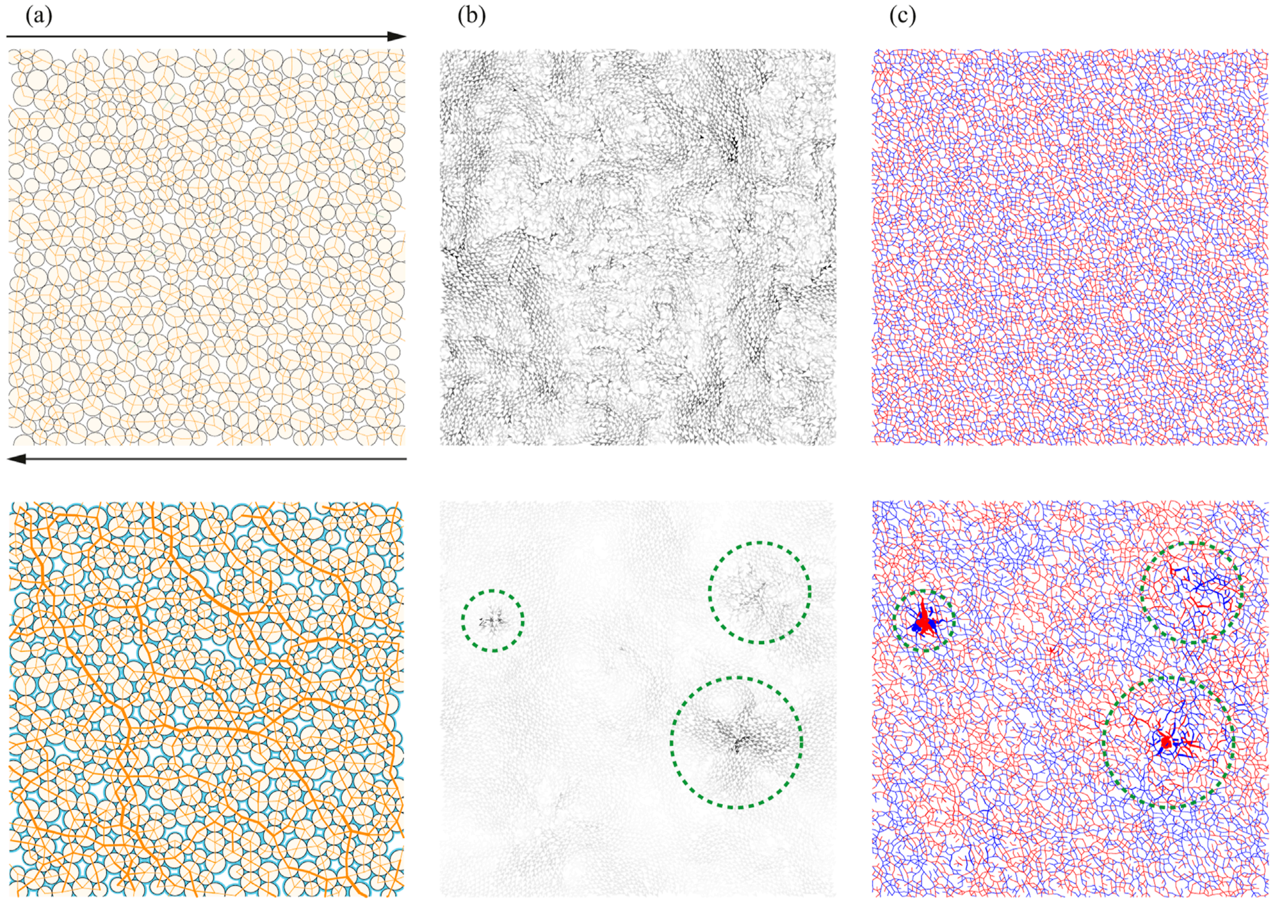

FIGURE 2
(A) Snapshots of soft cohesive particles under shear, where the particles (circles) are sheared along the horizontal arrows in the top panel. The system size and packing fraction of the particles are given by $N = 512$ and $\phi = 0.82$, respectively. The dimensionless parameters, $a = 10^{-6}$ (top) and 10^{-2} (bottom), are used for the cohesive interaction, Equation 1. The solid lines represent force-chain networks, where their width is proportional to the repulsive force, $k\delta_{ij} > 0$, between the particles in contact. The sticky layer (magnified by 10 times) is visualized by the shaded region around each particle. **(B)** Non-affine displacements of the particles in single stress drop events, where ϕ and a are as in **(A)**. The system size is $N = 8192$ and the avalanche sizes are given by $S \simeq 2.0 \times 10^{-4} kd_0^2$ (top) and $2.2 \times 10^{-2} kd_0^2$ (bottom). In the bottom panel, the green dashed circles show localized regions of non-affine displacements. **(C)** Changes of force-chain networks during single slip avalanches, where ϕ, a, N, and S are as in **(B)**. The red (blue) solid lines represent the increase (decrease) of the repulsive force, $k\delta_{ij} > 0$, where their width is proportional to the magnitude of force changes. In the bottom panel, the green dashed circles indicate the localized regions of force changes.

(Figure 3B left), the particles tend to be over-compressed such that $\hat{\delta}_{ij} > 0$, where the force is repulsive, i.e., $f_{ij}^{c} > 0$. In the compressive direction, the product of x- and y-components of the normal unit vector is negative, $n_{ijx}n_{ijy} < 0$, so that such a configuration increases σ (see Equation 2). On the other hand, if the particles are aligned in the decompressive direction (Figure 3B right), the particles tend to be connected by the sticky layer, where the force is attractive, i.e., $f_{ij}^{c} < 0$. Since $n_{ijx}n_{ijy} > 0$ in the decompressive direction, such a configuration also increases σ. Therefore, both cases contribute to the increase of σ so that the stronger the cohesive interactions are, the larger the shear stress is.

3.3 Mean shear stress and stress fluctuations

To quantify the influence of cohesive forces on the shear stress σ, we analyze the mean value of σ in a steady state. As shown in the stress-strain curve (Figure 3A), σ fluctuates around its mean value if the shear strain exceeds unity, $\gamma > 1$. Thus, we calculate the mean shear stress $\langle\sigma\rangle$ as the average of σ in the strain interval, $1 < \gamma < 11$. Though previous works of the rheology of soft frictionless particles focused on the divergence of viscosity near the jamming transition [70–74], we show the dependence of $\langle\sigma\rangle$ on the range of cohesive interactions a and packing fraction of the particles ϕ. Figure 4A plots $\langle\sigma\rangle$ as a function of a, where ϕ increases as listed in the legend. It is obvious that $\langle\sigma\rangle$ increases with ϕ because the system becomes rigid with the increase of density [2]. To describe the dependence of $\langle\sigma\rangle$ on a, we note that the magnitude of cohesive force is divided into two parts as $f_{ij}^{c} = g_{ij} + h_{ij}a$, where g_{ij} and h_{ij} do not include a (see Equation 1). According to the Born-Huang expression, Equation 2, we find that the shear stress is decomposed as

$$\sigma = \sigma_0 + \sigma_1 a, \tag{3}$$

where σ_0 and σ_1 are independent of a (see SM). Our numerical results of $\langle\sigma\rangle$ are well described by $\langle\sigma\rangle = \langle\sigma_0\rangle + \langle\sigma_1\rangle a$

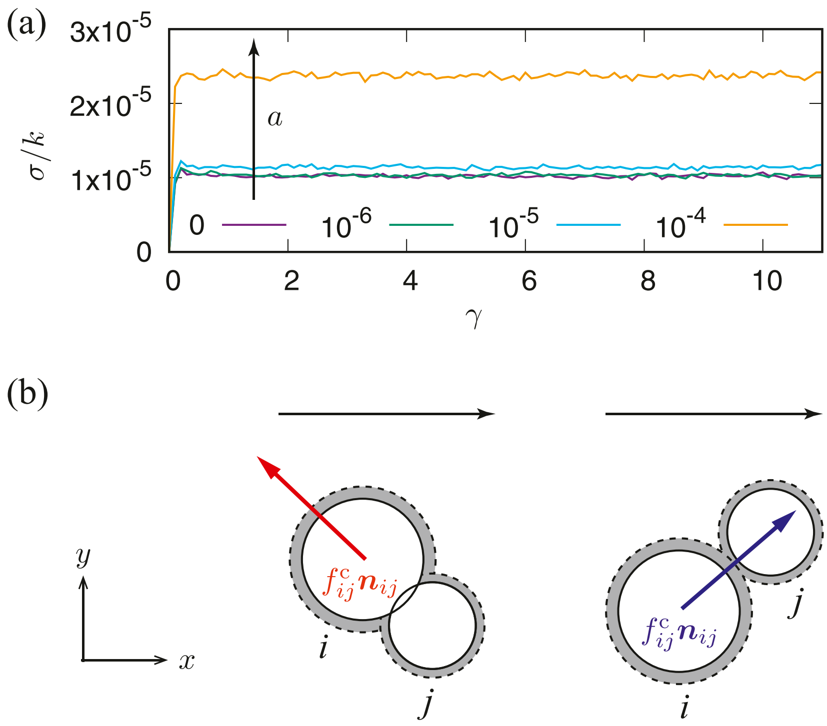

FIGURE 3
(A) *Stress-strain curves*, σ vs γ, where the system size is $N = 131072$ and the packing fraction is given by $\phi = 0.82$. The range of cohesive interactions a increases as listed in the legend (indicated by the vertical arrow). **(B)** Typical configurations of the particles aligned in the compressive (left) and decompressive (right) directions, where the system is sheared along the x-axis (as indicated by the horizontal arrows). The i-th (large) and j-th (small) particles are in contact, where the shaded regions represent sticky layers. The force is positive, $f^c_{ij} > 0$, and the product of x- and y-components of the normal unit vector is negative, $n_{ijx}n_{ijy} < 0$ (left), while $f^c_{ij} < 0$ and $n_{ijx}n_{ijy} > 0$ (right). In both cases, $-f^c_{ij}r_{ij}n_{ijx}n_{ijy} > 0$ so that the configurations not only in the compressive direction (left) but also in the decompressive direction (right) contribute to the increase of σ (Equation 2).

(dashed lines in Figure 4A) if we use the coefficients, $\langle\sigma_0\rangle$ and $\langle\sigma_1\rangle$, for fitting parameters.

In addition to the mean shear stress $\langle\sigma\rangle$, we analyze fluctuations of the shear stress in a steady state. We quantify stress fluctuations by the variance, $\langle\delta\sigma^2\rangle = \langle\sigma^2\rangle - \langle\sigma\rangle^2$, where the ensemble averages $\langle\dots\rangle$ are taken over the data in the strain interval, $1 < \gamma < 11$. Figure 4B shows the variance $\langle\delta\sigma^2\rangle$ as a function of a, where the packing fraction ϕ increases as in Figure 4A. As can be seen, the variance is also a monotonically increasing function of a and ϕ. To explain the dependence of $\langle\delta\sigma^2\rangle$ on a, we substitute $\sigma = \sigma_0 + \sigma_1 a$ into $\langle\delta\sigma^2\rangle = \langle\sigma^2\rangle - \langle\sigma\rangle^2$. Neglecting the correlation between σ_0 and σ_1 as $\langle\sigma_0\sigma_1\rangle \approx \langle\sigma_0\rangle\langle\sigma_1\rangle$, we find that the variance is quadratic in a as $\langle\delta\sigma^2\rangle \approx \langle\delta\sigma_0^2\rangle + \langle\delta\sigma_1^2\rangle a^2$ (see SM). Our numerical results are well described by $\langle\delta\sigma^2\rangle = \langle\delta\sigma_0^2\rangle + \langle\delta\sigma_1^2\rangle a^2$ (dashed lines in Figure 4B), where $\langle\delta\sigma_0^2\rangle$ and $\langle\delta\sigma_1^2\rangle$ are used for fitting parameters.

3.4 Slip avalanches

In contrast to the mean shear stress and stress fluctuations (Section 3.3), *slip avalanches* characterize plastic responses of the system to simple shear deformations. Closely looking at the stress-strain curve in a steady state (Figure 3A), one observes that the shear stress increasing with the shear strain suddenly drops to a lower value. Such a stress drop event, or slip avalanche, makes the mean shear stress (in a steady state) $\langle\sigma\rangle$ constant such that the shear stress fluctuates around it. A stress drop amplitude for a single slip avalanche is introduced as

$$\Delta\sigma \equiv \sigma(\gamma_0) - \sigma(\gamma_0 + T) > 0, \tag{4}$$

where the shear stress σ starts decreasing at the strain γ_0 and stops decreasing at $\gamma_0 + T$. The duration of a slip avalanche is given by dimensionless *avalanche duration* T and the so-called *avalanche size* is defined as $S \equiv L^2\Delta\sigma$ [33].

We calculate an average of avalanche sizes as $\langle S\rangle$ when the system is in a steady state ($\gamma > 1$). While previous studies paid much attention to finite size effects on the mean avalanche size [29, 35, 75, 76, 77, 78, 79, 80], we focus on the dependence of $\langle S\rangle$ on the range of cohesive interactions a and packing fraction of the particles ϕ. Figure 4C displays double logarithmic plots of $\langle S\rangle$ and a, where ϕ increases as listed in the legend of Figure 4A. In this figure, we average S over 10^6 stress drop events in a steady state. Similar to the mean shear stress and stress fluctuations (Figures 4A, B), $\langle S\rangle$ is also a monotonically increasing function of a and ϕ. Substituting the decomposition, Equation 3, into Equation 4, we find that the avalanche size is decomposed as $S = S_0 + S_1 a$, where S_0 and S_1 are

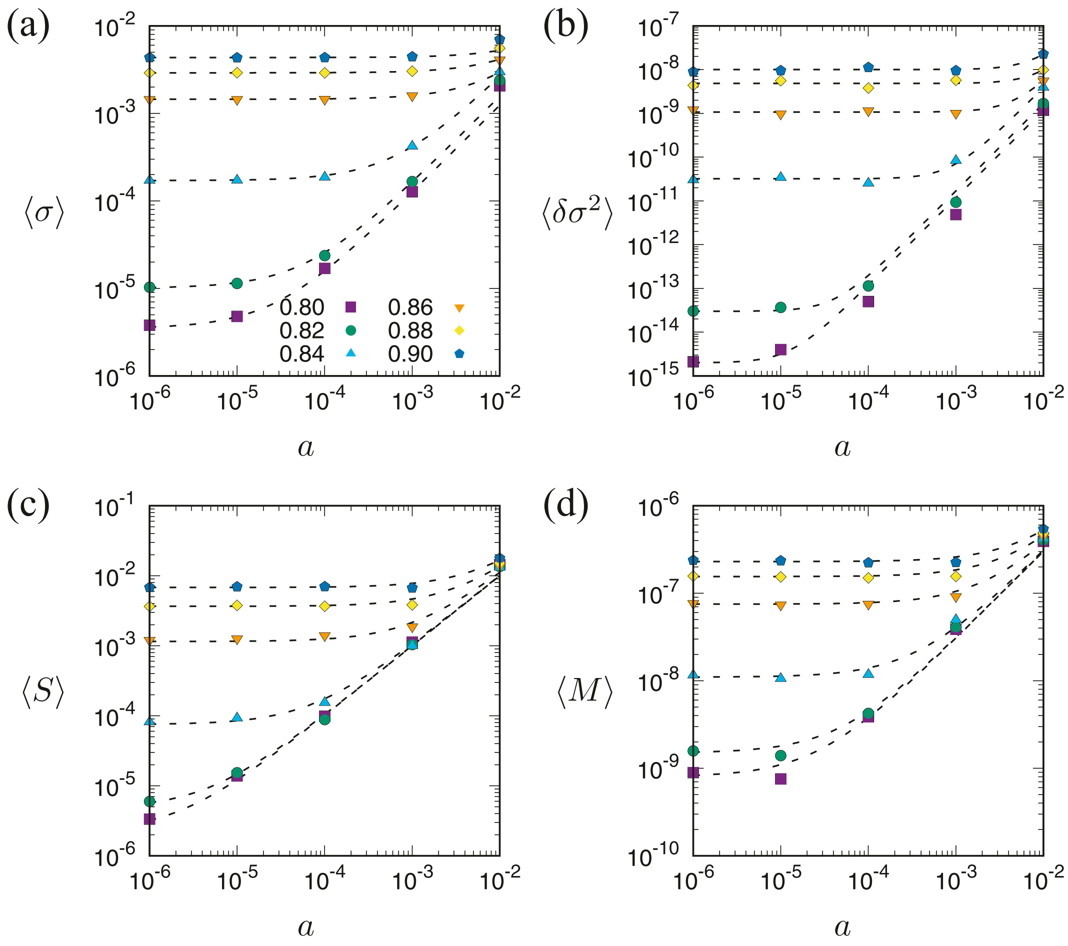

FIGURE 4
Double logarithmic plots of **(A)** the mean shear stress, **(B)** variance of the shear stress, **(C)** mean avalanche size, and **(D)** mean maximum stress drop rate as functions of the dimensionless parameter a. The packing fraction increases as listed in the legend of **(A)**, where the system size, $N = 131072$, is used for MD simulations. The dashed lines indicate fitting functions (see the main text and SM).

independent of a (see SM). Our numerical results are well fitted to $\langle S\rangle = \langle S_0\rangle + \langle S_1\rangle a$ (dashed lines in Figure 4C) if we use $\langle S_0\rangle$ and $\langle S_1\rangle$ for fitting parameters.

The slip avalanche defined as Equation 4 can be rephrased as the stress drop rate is negative, i.e., $d\sigma/d\gamma < 0$, in the strain interval between γ_0 and $\gamma_0 + T$. Because the dimensionless avalanche duration is finite, $T > 0$, we can calculate the *maximum stress drop rate* as $M \equiv (-d\sigma/d\gamma)_{\max}$ for each stress drop event. Figure 4D shows double logarithmic plots of the mean maximum stress drop rate $\langle M\rangle$ and a, where we took 10^6 ensemble averages of M in a steady state and ϕ increases as listed in the legend of Figure 4A. Similar to the mean avalanche size (Figure 4C), $\langle M\rangle$ also monotonously increases with a and ϕ. Because of Equation 3, the maximum stress drop rate is decomposed as $M = M_0 + M_1 a$ with the a-independent coefficients, M_0 and M_1 (see SM). We find that our numerical results are well fitted to $\langle M\rangle = \langle M_0\rangle + \langle M_1\rangle a$ (dashed lines in Figure 4D) if we use $\langle M_0\rangle$ and $\langle M_1\rangle$ for fitting parameters.

Note that we cannot see a clear trend in the mean value of dimensionless avalanche duration $\langle T\rangle$, where $\langle T\rangle$ slightly increases with a (see SM).

3.5 Scaling laws of slip avalanches

It was predicted by the MF theory of slip avalanches that both T and M scale as the square root of S, i.e., $T \sim S^{1/2}$ and $M \sim S^{1/2}$, in the scaling regime [19]. To examine whether the MF predictions are applicable to our system, we make scatter plots of S, T, and M from the data of 10^6 slip avalanches in a steady state. Figure 5A shows the scatter plots of S and T (left), and S and M (right), where each dot corresponds to each slip avalanche. The symbols (circles) are the averages of T and M in each bin of S. As can be seen, both T and M tend to increase with S if the avalanche size is large enough, e.g., $S \gtrsim 10^{-4} k d_0^2$ or $S \gtrsim \langle S\rangle$. In our MD simulations, the lower bound of dimensionless avalanche duration is given by the strain increment as $T \geq \Delta\gamma = 10^{-7}$. Therefore, if the dimensionless avalanche duration is the smallest, $T = \Delta\gamma$, the maximum stress drop rate is given by $M = \Delta\sigma/\Delta t = S/(L^2\Delta t)$, where M is proportional to S. The solid line in Figure 5A (right) indicates the proportionality, $M \propto S$, for sufficiently small avalanches.

We show that the scaling laws of S, T, and M can be confirmed even if the cohesive forces exist. Figure 5B displays the averages

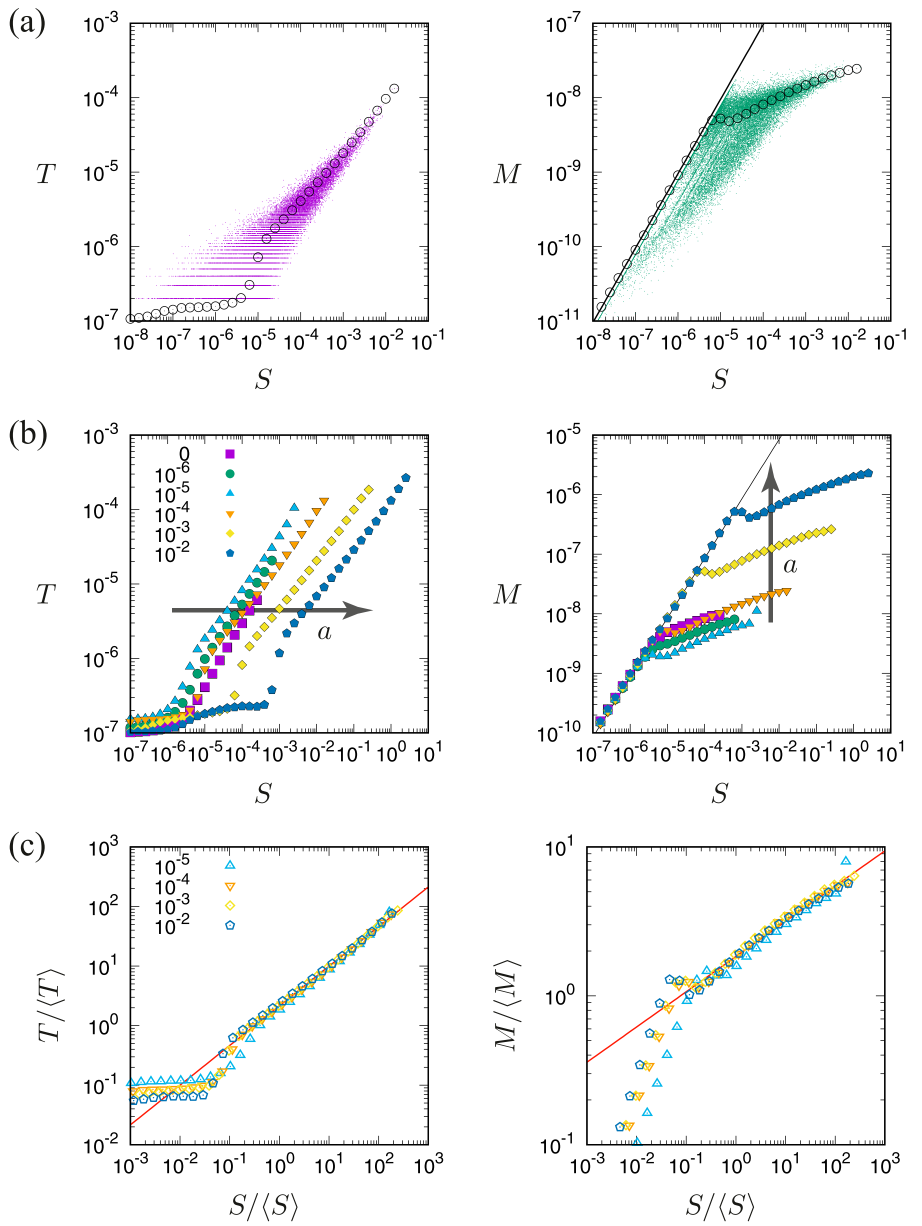

FIGURE 5
(A) (Left) A scatter plot of the avalanche size S and dimensionless avalanche duration T, where each symbol (circle) represents an average of T in each bin of S. (Right) A scatter plot of S and maximum stress drop rate M, where each symbol (circle) is an average of M in each bin of S. The dimensionless parameter is given by $a = 10^{-4}$. The solid line in the right panel indicates the proportionality, $M \propto S$. **(B)** Double logarithmic plots of T (left) and M (right) as functions of S, where a increases as listed in the legend and indicated by the arrows. The solid line in the right panel indicates $M \propto S$. **(C)** Scaling laws of T (left) and M (right), where the solid lines represent Equations 5, 6. The dimensionless parameter a ($\geq 10^{-5}$) increases as listed in the legend. In **(A–C)**, the system size and packing fraction are given by $N = 131072$ and $\phi = 0.82$, respectively.

of T (left) and M (right) in each bin of S, where we increase the dimensionless parameter a as listed in the legend (indicated by the arrows). One can see that both T and M monotonically increase with S if the avalanche size is large enough as $S \gtrsim \langle S\rangle$. To examine the scaling laws of S, T, and M, we plot $T/\langle T\rangle$ and $M/\langle M\rangle$ as functions of $S/\langle S\rangle$ in Figure 5C. We find that all the data in $S/\langle S\rangle \geq 1$ are nicely collapsed if the dimensionless parameter is not infinitesimal, $a \geq 10^{-5}$. The solid lines represent scaling laws.

$$\frac{T}{\langle T\rangle} \sim \left(\frac{S}{\langle S\rangle}\right)^{\mu}, \tag{5}$$

$$\frac{M}{\langle M\rangle} \sim \left(\frac{S}{\langle S\rangle}\right)^{\zeta}, \tag{6}$$

where the exponents, $\mu \simeq 0.66$ and $\zeta \simeq 0.24$, estimated from the data of $a = 10^{-2}$ are different from the MF prediction, $1/2$. Therefore, the scaling laws, Eqs. (5) and (6), can be confirmed for $a \geq 10^{-5}$, where the exponents, μ and ζ, are quite insensitive to the range of cohesive interactions. Note that the influence of cohesive forces is included in the averages, $\langle S\rangle$, $\langle T\rangle$, and $\langle M\rangle$ (see Figure 4).

In SM, we show that Equations 5, 6 hold for large avalanches, $S/\langle S\rangle \geq 1$, regardless of the packing fraction ϕ, where we estimate the exponents, μ and ζ, for each value of ϕ. We also examine finite size effects on the scaling, Equations 5, 6, and confirm that the scaling laws are well established if the system size is large enough (see SM).

3.6 Statistics of slip avalanches

In contrast to the mean values, $\langle S\rangle$ and $\langle T\rangle$, the occurrence of slip avalanches is quantified by the probability distribution functions (PDFs) of avalanche sizes and dimensionless avalanche duration, i.e., $P(S)$ and $P(T)$. The MF theory predicts the power-law decay of the PDFs as $P(S) \sim S^{-\tau}$ and $P(T) \sim T^{-\kappa}$ in the scaling regimes, where the power-law exponents are given by $\tau = 3/2$ and $\kappa = 2$ [12–15]. The power-law decay was validated by many experiments of granular materials [16–19], metallic glasses [22–25], etc. However, some simulations disagree with the MF predictions and there has been much debate as mentioned in the Introduction (Section 1). Figure 6 shows double logarithmic plots of the PDFs, (a) $P(S)$ and (b) $P(T)$, where the dimensionless parameter a increases as listed in the legend of (a) (indicated by the arrows). Increasing a, we observe qualitative changes in the shapes of the PDFs, e.g., their tails extend to higher values of S and T. In addition, our numerical results are clearly different from the MF predictions, $P(S) \sim S^{-3/2}$ and $P(T) \sim T^{-2}$ (dashed lines).

To analyze the shapes of $P(S)$ and $P(T)$, we scale them by the mean values, $\langle S\rangle$ and $\langle T\rangle$, respectively. Figure 7A displays the scaled PDFs of avalanche sizes. If the range of cohesive interactions is not sufficiently small ($a \geq 10^{-5}$), the scaled PDFs are well collapsed on top of each other. We describe the tails of the scaled PDFs as

$$\langle S\rangle P(S) \sim \left(\frac{S}{\langle S\rangle}\right)^{-\tau} e^{-S/S_c} \tag{7}$$

(solid line), where the cut-off value [32], $S_c \equiv \langle S^2\rangle/\langle S\rangle$, is extracted from the simulation with $a = 10^{-2}$. The power-law exponent in Equation 7 is estimated from the data of $a = 10^{-2}$ as $\tau \simeq 1.1$ which is smaller than the MF prediction, 3/2. Figure 7B shows the scaled PDFs of dimensionless avalanche duration, where all the data are nicely collapsed if $a \geq 10^{-5}$. The solid line indicates

$$\langle T\rangle P(T) \sim \left(\frac{T}{\langle T\rangle}\right)^{-\kappa} e^{-T/T_c} \tag{8}$$

with $T_c \equiv \langle T^2\rangle/\langle T\rangle$, where we find an extremely small exponent, $\kappa \simeq 1.1$, from the data of $a = 10^{-2}$. Thus, the power-law scaling of the PDFs, Equations 7, 8, can be confirmed for $a \geq 10^{-5}$, where the exponents, τ and κ, are almost independent of the range of cohesive interactions. The influence of cohesive forces is included in the averages, $\langle S\rangle$ and $\langle T\rangle$, and cutoff values, S_c and T_c (data are not shown).

Though the power-law exponents, τ and κ, in Equations 7, 8 are smaller than the MF predictions, they are consistent with the exponent μ for the scaling law, Equation 5. Let us derive a relation

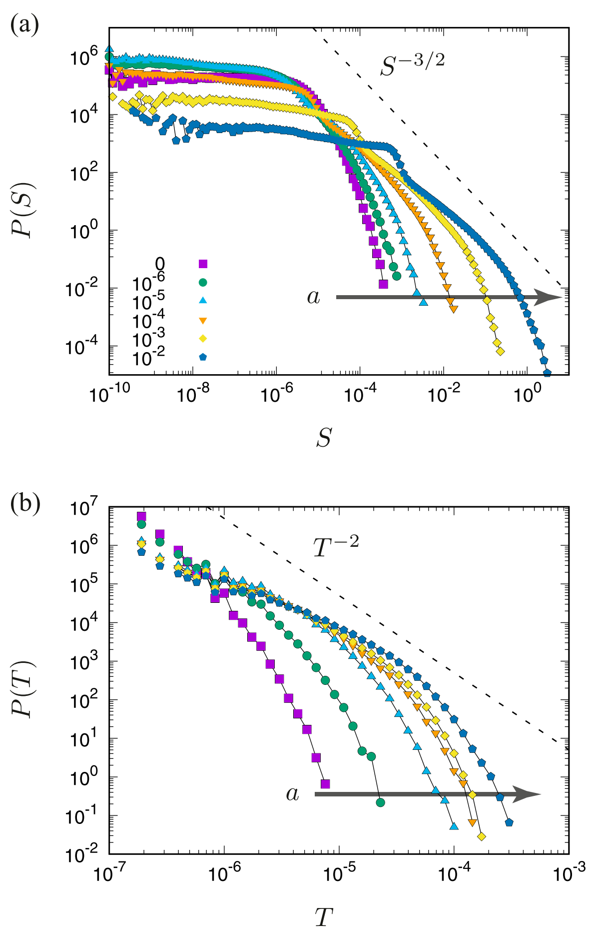

FIGURE 6
Double logarithmic plots of the PDFs of **(A)** avalanche sizes, $P(S)$, and **(B)** dimensionless avalanche duration, $P(T)$. The range of cohesive interactions a increases as listed in the legend of **(A)** and indicated by the arrows. The dashed lines represent the MF predictions, i.e., **(A)** $S^{-3/2}$ and **(B)** T^{-2}. The system size and packing fraction are as in Figure 5.

between the power-law exponents as follows. The probability that the avalanche size is in the range between S and $S + dS$ is given by $P(S)dS$. On the other hand, the probability that the dimensionless avalanche duration is in the range between T and $T + dT$ is $P(T)dT$. Assuming the one-to-one correspondence between S and T, we equate these probabilities as $P(S)dS = P(T)dT$. This means that the PDFs are related to each other as

$$P(S) = P(T)\frac{dT}{dS}. \tag{9}$$

Because the dimensionless avalanche duration T obeys the scaling law, Equation 5, in the scaling regime, the derivative in Equation 9 scales as $dT/dS \sim \mu S^{\mu-1}$. Thus, substituting the power-law decay, $P(S) \sim S^{-\tau}$ and $P(T) \sim T^{-\kappa}$, into Equation 9, we find $S^{-\tau} \sim T^{-\kappa} \times \mu S^{\mu-1} \sim S^{(1-\kappa)\mu-1}$. Therefore, the exponent τ is related to the others as

$$\tau = (\kappa - 1)\mu + 1. \tag{10}$$

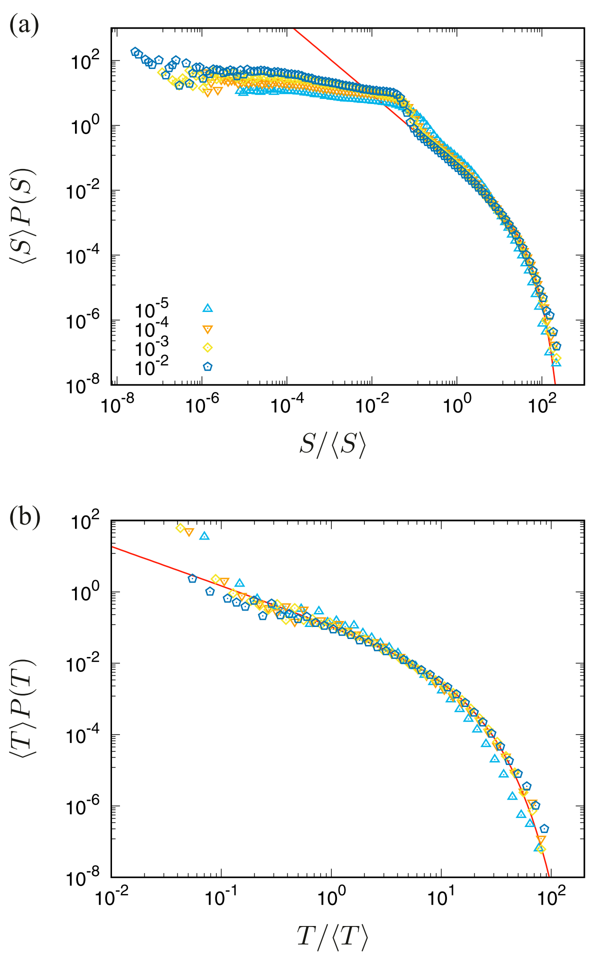

FIGURE 7
Double logarithmic plots of the scaled PDFs, **(A)** $\langle S\rangle P(S)$ and **(B)** $\langle T\rangle P(T)$, where the dimensionless parameter $a \geq 10^{-5}$ increases as listed in the legend of **(A)**. The solid lines are fits to the tails of the scaled PDFs (see main text). The system size and packing fraction are as in Figure 5.

The MF predictions, i.e., $\tau = 3/2$, $\kappa = 2$, and $\mu = 1/2$, satisfy Equation 10, while our results, $\tau \simeq 1.1$, $\kappa \simeq 1.1$, and $\mu \simeq 0.66$, are also consistent with (Equation 10)[2].

In SM, we analyze the effect of packing fraction ϕ on the scaled PDFs, where we estimate the exponents, τ and κ, and examine the relation, Equation 10, for each value of ϕ.

In addition, we examine finite size effects on the tails of the scaled PDFs, where Equations 7, 8 well explain our numerical results unless the system size is extremely small (see SM).

3.7 Particle rearrangements during a slip avalanche

On a microscopic scale, a slip avalanche is triggered by rearrangements of the particles under shear. In our MD simulations, particle displacements (in each strain step) can be decomposed as $\boldsymbol{u}_i = \Delta\gamma y_i \boldsymbol{e}_x + \delta\boldsymbol{u}_i$ $(i = 1, \ldots, N)$, where $\boldsymbol{e}_x$ is a unit vector parallel to the x-axis. The first term $\Delta\gamma y_i \boldsymbol{e}_x$ represents an affine displacement, whereas the second term $\delta\boldsymbol{u}_i$ is a non-affine displacement. The non-affine displacements $\delta\boldsymbol{u}_i$ $(i = 1, \ldots, N)$ represent the particle rearrangements under shear [81–83] and suppress the increase of shear stress [84]. It is thus expected that the non-affine displacements are relevant to the avalanche size S. To analyze the particle rearrangements during a single slip avalanche, we integrate the non-affine displacements over the strain interval between γ_0 and $\gamma_0 + T$ as $\delta\bar{\boldsymbol{u}}_i \equiv \int_{\gamma_0}^{\gamma_0+T} \delta\boldsymbol{u}_i(\gamma)d\gamma$. Figure 2B shows spatial distributions of $\delta\bar{\boldsymbol{u}}_i$ $(i = 1, \ldots, N)$ (arrows), where the gray scale indicates the magnitude of $\delta\bar{\boldsymbol{u}}_i$. If the range of cohesive interactions is small ($a = 10^{-6}$), the spatial distributions of $\delta\bar{\boldsymbol{u}}_i$ are homogeneous (Figure 2B top), where we observe "collective rearrangements" of the particles everywhere in the system [81–83]. In contrast, if the range of cohesive interactions is large ($a = 10^{-2}$), the spatial distributions are typically localized (Figure 2B bottom), where characteristic "quadrupole structures" of $\delta\bar{\boldsymbol{u}}_i$ can be seen in the green circles [28, 29, 33].

Note that particle rearrangements are directly linked to restructuring of force-chain networks [85, 86]. Because we calculate the stress tensor by the Born-Huang expression (Eq. (2)), a stress drop event is a consequence of restructuring of force-chains. Figure 2C visualizes the changes of force-chain networks during a slip avalanche. The red (blue) solid lines represent the increase (decrease) of the repulsive forces, $k\delta_{ij} > 0$, where the particles, i and j, are in contact before the slip avalanche. If cohesive interactions are weak (top), the restructuring of force-chains is not localized. However, if cohesive interactions are strong (bottom), the restructuring is localized at which the cumulative non-affine displacements $\delta\bar{\boldsymbol{u}}_i$ are localized (green circles).

To quantitatively compare the non-affine displacements with the avalanche size S, we introduce the *mean squared displacement* (MSD) during a slip avalanche [87] as

$$\Delta^2 \equiv \frac{1}{N}\sum_{i=1}^{N} \delta\bar{\boldsymbol{u}}_i^2. \tag{11}$$

Figure 8A displays double logarithmic plots of the average of MSD $\langle\Delta^2\rangle$ and the dimensionless parameter a, where we averaged Equation 11 over 10^6 slip avalanches in a steady state. Similar to the mean values in Figure 4, $\langle\Delta^2\rangle$ monotonously increases with a and the packing fraction ϕ (symbols). We also quantify the localization of particle rearrangements by the *participation ratio*,

$$p_r \equiv \frac{\left(\sum_{i=1}^{N} \delta\bar{\boldsymbol{u}}_i^2\right)^2}{N\sum_{i=1}^{N} |\delta\bar{\boldsymbol{u}}_i|^4}. \tag{12}$$

Figure 8B shows the mean participation ratio $\langle p_r\rangle$ as a function of a, where we took 10^6 ensemble averages of Equation 12 in a steady state. Different from the average of MSD (and other averages in Figure 4), $\langle p_r\rangle$ *decreases* with the increases of a and ϕ (symbols). If $\phi > \phi_J \simeq 0.8433$ (see Section 3.1 for the jamming transition density ϕ_J), the mean participation ratio is extremely small, $\langle p_r\rangle \simeq 0.1$, such that the rearrangements during a slip avalanche are localized regardless of cohesive forces. However, if $\phi < \phi_J$ and the range of cohesive interactions is small, the rearrangements are not localized, e.g., $\langle p_r\rangle \simeq 0.5$ for $\phi = 0.82$ and $a \leq 10^{-4}$. Interestingly, $\langle p_r\rangle$ starts decreasing if a exceeds 10^{-4} and drops to $\langle p_r\rangle \simeq 0.1$ if $a = 10^{-2}$.

2 Substituting our estimates, $\kappa \simeq 1.1$ and $\mu \simeq 0.66$, into Equation 10, we find $\tau \simeq 1.066$ which is approximately equal to our result, $\tau \simeq 1.1$.

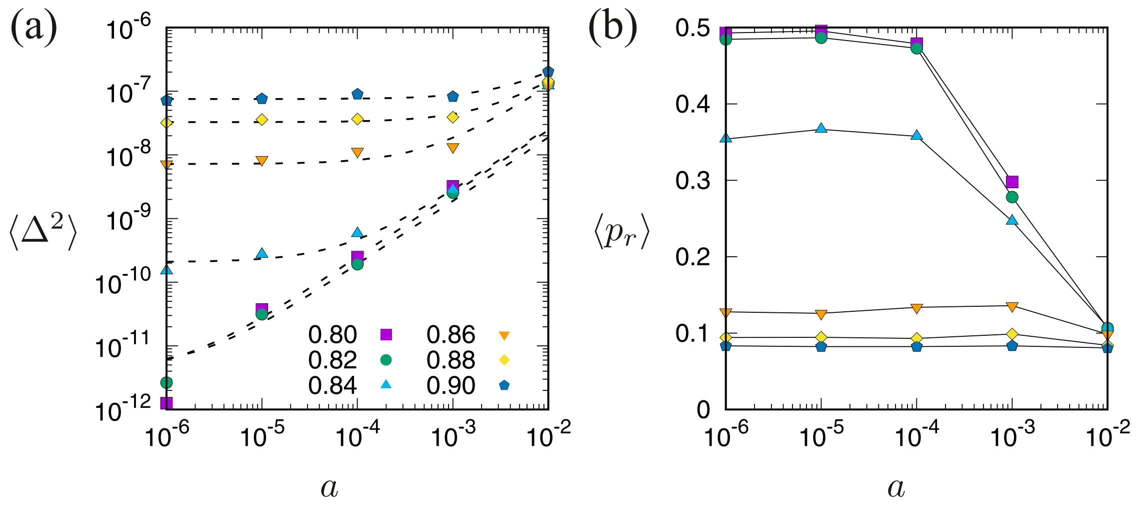

FIGURE 8
Double logarithmic plots of **(A)** the average of MSD and **(B)** mean participation ratio as functions of the dimensionless parameter a. The packing fraction increases as listed in the legend of **(A)**, where the system size, $N = 131072$, is used for MD simulations. The dashed lines in **(A)** are guides to the eyes (linear functions of a fitted to the data).

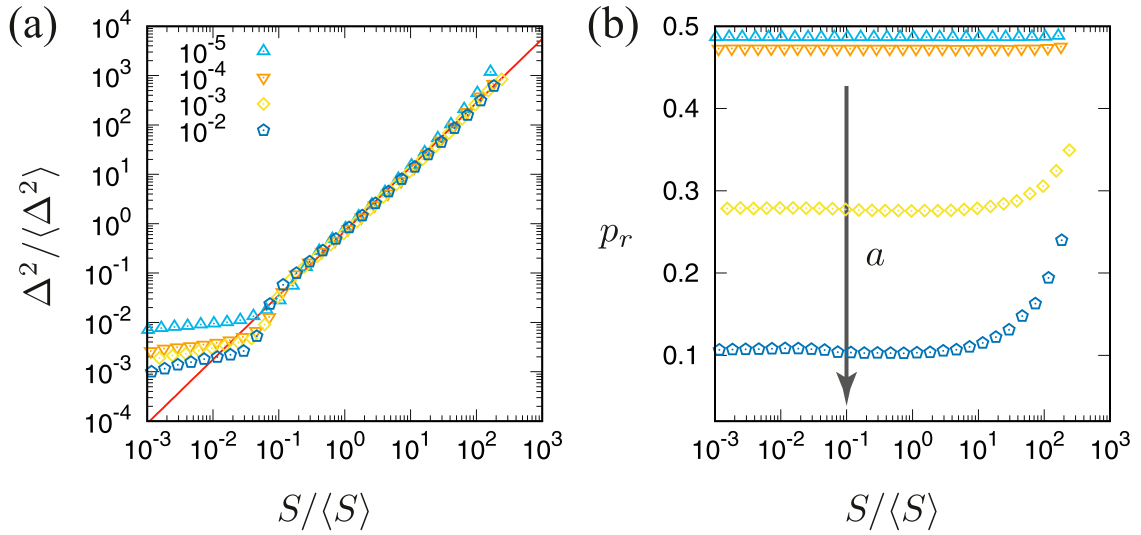

FIGURE 9
(A) Double logarithmic plots of the scaled avalanche size $S/\langle S\rangle$ and scaled MSD $\Delta^2/\langle\Delta^2\rangle$, where the solid line indicates the scaling law, Equation 13. **(B)** Semi-logarithmic plots of $S/\langle S\rangle$ and the participation ratio p_r. In **(A)** and **(B)**, the dimensionless parameter a increases from 10^{-5} as listed in the legend of **(A)** and indicated by the arrow in **(B)**. The system size and packing fraction are as in Figure 5.

Therefore, if the thickness of sticky layer increases to 1% of particle diameter, the rearrangements during a slip avalanche are mostly localized regardless of ϕ.

Finally, we show that the MSD is relevant to the avalanche size S, while the localization of non-affine displacements is unrelated to S. Figure 9A displays double logarithmic plots of the scaled MSD $\Delta^2/\langle\Delta^2\rangle$ and scaled avalanche size $S/\langle S\rangle$, where each symbol represents an average of Δ^2 in each bin of S. As in the cases of dimensionless avalanche duration T and maximum stress drop rate M (Figure 5), all the data of $\Delta^2/\langle\Delta^2\rangle$ in $S/\langle S\rangle \geq 1$ are well collapsed if the range of cohesive interactions is not infinitesimal, $a \geq 10^{-5}$. From our numerical results, we find the scaling law of MSD (solid line) as

$$\frac{\Delta^2}{\langle\Delta^2\rangle} \sim \left(\frac{S}{\langle S\rangle}\right)^{\lambda}, \tag{13}$$

where the exponent estimated from the data of $a = 10^{-2}$ is $\lambda \simeq 1.30$. The positive exponent, $\lambda > 0$, means that a large avalanche, $S \geq \langle S\rangle$, is accompanied by a large amount of particle rearrangements. In addition, Equation 13 may be explained by the scaling law of T

(Equation 5) as follows. If the magnitude of non-affine displacement in each strain step $\Delta\gamma$ is given by l (on average), the magnitude of non-affine displacement during a slip avalanche is Tl. The MSD is then estimated as $\Delta^2 \sim (Tl)^2$. Substituting Equation 5, we find $\Delta^2/\langle\Delta^2\rangle \sim (T/\langle T\rangle)^2 \sim (S/\langle S\rangle)^{2\mu}$, where the exponent, $2\mu \simeq 1.32$, is close to $\lambda \simeq 1.30$. In contrast, the participation ratio p_r is flat over the whole range of $S/\langle S\rangle$ if $a \le 10^{-4}$ (Figure 9B)[3]. If $a \ge 10^{-3}$, p_r is constant unless the avalanche size is extremely large and slightly increases with extremely large avalanches (Figure 9B). However, p_r is much more sensitive to a and its correlation with S is not significant.

In SM, we confirm that the scaling law, Equation 13, holds in $S/\langle S\rangle \ge 1$ regardless of the packing fraction ϕ. We also show that, if $\phi > \phi_J$, the cohesive interactions are not important and the non-affine displacements during a slip avalanche are mostly localized ($p_r \simeq 0.1$) except for extremely large avalanches, $S/\langle S\rangle > 10$. Furthermore, we examine finite size effects on the scaling law and participation ratio and find that Equation 13 is well established unless the system size is too small (see SM).

4 Discussion and conclusion

In this study, we have examined mechanical responses of soft cohesive particles to simple shear deformations by MD simulations. In our cohesive contact model [48–50, 53, 54], the range of cohesive interactions is controlled by the dimensionless parameter a (Equation 1). We found that, if a is large enough, the particles are locally jammed or aggregate each other as if the system exhibits "gelation" (Figure 2A). The shear stress in a steady state, i.e., the shear strength, and the averages of avalanche size and maximum stress drop rate are increasing functions of a (and the packing fraction of the particles ϕ) (Figure 4). Since the shear stress is given by a linear function of a (Equation 3), the avalanche size and maximum stress drop rate are also linear functions of a. We showed that the scaling laws of dimensionless avalanche duration and maximum stress drop rate (Equations 5, 6) are well established even if the cohesive forces exist (Figure 5). In addition, another scaling law of MSD (Equation 13) was confirmed as the consequence of the scaling law of dimensionless avalanche duration. We also found that the PDFs of avalanche sizes and dimensionless avalanche duration are well described by the power-law scaling (Equations 7, 8). However, the power-law exponents extracted from the data of PDFs do not agree with the MF predictions but rather are consistent with the scaling law of dimensionless avalanche duration (Equation 10). Note that all the exponents for the scaling laws and the PDFs are independent of the range of cohesive interactions (if $a \ge 10^{-5}$), while the influence of cohesive forces is included in the averages and cutoff values.

One of the characteristic features of soft cohesive particles under shear is the localization of particle rearrangements. We quantified the localization by the participation ratio of non-affine displacements and found that, if the system is less dense as $\phi < \phi_J$, the particle rearrangements during a slip avalanche are strongly dependent on the range of cohesive interactions a (Figure 8B). Interestingly, the participation ratio does not correlate significantly with the avalanche size (Figure 9B) and the non-affine displacements, if localized, exhibit characteristic quadrupole structures (Figure 2B). A further analysis is necessary to unveil the mechanism of the localization, which is left for future work.

In our MD simulations, we assumed that the system is in a pendular state, where the cohesive force between the particles is pairwise. However, if the liquid content increases, the system transitions to a *funicular* or *capillary state*, where more than two particles interact through the liquid [3,4]. We did not implement such many body interactions into our model though their effects on avalanches are interesting to know. In addition, in real granular materials, cohesive forces are intrinsically history-dependent [57]. Therefore, the influence of *hysteresis* in cohesive contacts has to be examined in future. Moreover, the effect of particle shapes [47] and simulations in three dimensions are important for practical applications of this work.

In conclusion, the shear strength, force-chains, and particle rearrangements are strongly affected by cohesive forces if the system is less dense. The statistics of avalanches, such as the scaling laws and power-law distributions, are well established even if the system is cohesive though the scaling exponents are distinct from the MF predictions.

3 We confirmed that $p_r \simeq 0.5$ over the whole range of $S/\langle S\rangle$ even if $a = 0$ and 10^{-6} (data are not shown).

Data availability statement

The original contributions presented in the study are included in the article/Supplementary Material, further inquiries can be directed to the corresponding author.

Author contributions

KS: Conceptualization, Funding acquisition, Investigation, Visualization, Writing–original draft, Writing–review and editing.

Funding

The author(s) declare that financial support was received for the research, authorship, and/or publication of this article. This work was financially supported by the KAKENHI Grant No. 22K03459 from JSPS.

Conflict of interest

The author declares that the research was conducted in the absence of any commercial or financial relationships that could be construed as a potential conflict of interest.

Generative AI statement

The author(s) declare that no Generative AI was used in the creation of this manuscript.

Publisher's note

All claims expressed in this article are solely those of the authors and do not necessarily represent those of their affiliated organizations, or those of the publisher, the editors and the reviewers. Any product that may be evaluated in this article, or claim that may be made by its manufacturer, is not guaranteed or endorsed by the publisher.

Supplementary material

The Supplementary Material for this article can be found online at: https://www.frontiersin.org/articles/10.3389/fphy.2025.1548966/full#supplementary-material

References

1. Jeager H, Nagel S, Behringer R. Granular solids, liquids, and gases. *Rev Mod Phys* (1996) 68:1259–73. doi:10.1103/revmodphys.68.1259

2. Bonn D, Denn MM, Berthier L, Divoux T, Manneville S. Yield stress materials in soft condensed matter. *Rev Mod Phys* (2017) 89:035005. doi:10.1103/revmodphys.89.035005

3. Mitarai N, Nori F. Wet granular materials. *Adv Phys* (2006) 55:1–45. doi:10.1080/00018730600626065

4. Mitarai N, Nakanishi H. Simple model for wet granular materials with liquid clusters. *Eur Phys Lett* (2009) 88:64001. doi:10.1209/0295-5075/88/64001

5. Castellanos A. The relationship between attractive interparticle forces and bulk behaviour in dry and uncharged fine powders. *Adv Phys* (2005) 54:263–376. doi:10.1080/17461390500402657

6. Uhl JT, Pathak S, Schorlemmer D, Liu X, Swindeman R, Brinkman BAW, et al. Universal quake statistics: from compressed nanocrystals to earthquakes. *Sci Rep* (2015) 5:16493. doi:10.1038/srep16493

7. Hatano T, Narteau C, Shebalin P. Common dependence on stress for the statistics of granular avalanches and earthquakes. *Sci Rep* (2015) 5:12280. doi:10.1038/srep12280

8. Lherminier S, Planet R, Vehel VL, Simon G, Vanel L, Måløy KJ, et al. Continuously sheared granular matter reproduces in detail seismicity laws. *Phys Rev Lett* (2019) 122:218501. doi:10.1103/physrevlett.122.218501

9. Bak P, Tang C, Wiesenfeld K. Self-organized criticality: an explanation of the 1/*foise*. *Phys Rev Lett* (1987) 59:381–4. doi:10.1103/physrevlett.59.381

10. Sethna JP, Dahmen KA, Myers CR. Crackling noise. *Nature* (2001) 410:242–50. doi:10.1038/35065675

11. Fisher DS. Collective transport in random media: from superconductors to earthquakes. *Phys Rep* (1998) 301:113–50. doi:10.1016/s0370-1573(98)00008-8

12. Dahmen KA, Ben-Zion Y, Uhl JT. A simple analytic theory for the statistics of avalanches in sheared granular materials. *Nat Phys* (2011) 7:554–7. doi:10.1038/nphys1957

13. Fisher DS, Dahmen K, Ramanathan S, Ben-Zion Y. Statistics of earthquakes in simple models of heterogeneous faults. *Phys Rev Lett* (1997) 78:4885–8. doi:10.1103/physrevlett.78.4885

14. Dahmen KA, Ben-Zion Y, Uhl JT. Micromechanical model for deformation in solids with universal predictions for stress-strain curves and slip avalanches. *Phys Rev Lett* (2009) 102:175501. doi:10.1103/physrevlett.102.175501

15. Dahmen KA, Ertaş D, Ben-Zion Y. Gutenberg-Richter and characteristic earthquake behavior in simple mean-field models of heterogeneous faults. *Phys Rev E* (1998) 58:1494–501. doi:10.1103/physreve.58.1494

16. Geller DA, Ecke RE, Dahmen KA, Backhaus S. Stick-slip behavior in a continuum-granular experiment. *Phys Rev E* (2015) 92:060201. doi:10.1103/physreve.92.060201

17. Denisov DV, Lörincz KA, Uhl JT, Dahmen KA, Schall P. Universality of slip avalanches in flowing granular matter. *Nat Commun* (2016) 7:10641. doi:10.1038/ncomms10641

18. Denisov DV, Lörincz KA, Wright WJ, Hufnagel TC, Nawano A, Gu X, et al. Universal slip dynamics in metallic glasses and granular matter – linking frictional weakening with inertial effects. *Sci Rep* (2017) 7:43376. doi:10.1038/srep43376

19. Long AA, Denisov DV, Schall P, Hufnagel TC, Gu X, Wright WJ, et al. From critical behavior to catastrophic runaways: comparing sheared granular materials with bulk metallic glasses. *Granular Matter* (2019) 21:99. doi:10.1007/s10035-019-0946-y

20. Friedman N, Jennings AT, Tsekenis G, Kim JY, Tao M, Uhl JT, et al. Statistics of dislocation slip avalanches in nanosized single crystals show tuned critical behavior predicted by a simple mean field model. *Phys Rev Lett* (2012) 109:095507. doi:10.1103/physrevlett.109.095507

21. Csikor FF, Motz C, Weygand D, Zaiser M, Zapperi S. Dislocation avalanches, strain bursts, and the problem of plastic forming at the micrometer scale. *Science* (2007) 318:251–4. doi:10.1126/science.1143719

22. Antonaglia J, Wright WJ, Gu X, Byer RR, Hufnagel TC, LeBlanc M, et al. Bulk metallic glasses deform via slip avalanches. *Phys Rev Lett* (2014) 112:155501. doi:10.1103/physrevlett.112.155501

23. Antonaglia J, Xie X, Schwarz G, Wraith M, Qiao J, Zhang Y, et al. Tuned critical avalanche scaling in bulk metallic glasses. *Sci Rep* (2014) 4:4382. doi:10.1038/srep04382

24. Coleman JP, Meng F, Tsuchiya K, Beadsworth J, LeBlanc M, Liaw PK, et al. Effect of annealing on nanoindentation slips in a bulk metallic glass. *Phys Rev B* (2017) 96:134117. doi:10.1103/physrevb.96.134117

25. Sun BA, Yu HB, Jiao W, Bai HY, Zhao DQ, Wang WH. Plasticity of ductile metallic glasses: a self-organized critical state. *Phys Rev Lett* (2010) 105:035501. doi:10.1103/physrevlett.105.035501

26. Sheikh MA, Weaver RL, Dahmen KA. Avalanche statistics identify intrinsic stellar processes near criticality in KIC 8462852. *Phys Rev Lett* (2016) 117:261101. doi:10.1103/physrevlett.117.261101

27. Tewari S, Schiemann D, Durian DJ, Knobler CM, Langer SA, Liu AJ. Statistics of shear-induced rearrangements in a two-dimensional model foam. *Phys Rev E* (1999) 60:4385–96. doi:10.1103/physreve.60.4385

28. Maloney C, Lemaitre A. Subextensive scaling in the athermal, quasistatic limit of amorphous matter in plastic shear flow. *Phys Rev Lett* (2004) 93:016001. doi:10.1103/physrevlett.93.016001

29. Maloney CE, Lemaitre A. Amorphous systems in athermal, quasistatic shear. *Phys Rev E* (2006) 74:016118. doi:10.1103/physreve.74.016118

30. Bailey NP, Schiøtz J, Lemaitre A, Jacobsen KW. Avalanche size scaling in sheared three-dimensional amorphous solid. *Phys Rev Lett* (2007) 98:095501. doi:10.1103/physrevlett.98.095501

31. Heussinger C, Chaudhuri P, Barrat JL. Fluctuations and correlations during the shear flow of elastic particles near the jamming transition. *Soft Matter* (2010) 6:3050. doi:10.1039/b927228c

32. Shang B, Guan P, Barrat JL. Elastic avalanches reveal marginal behavior in amorphous solids. *Proc Natl Acad Sci USA* (2020) 117:86–92. doi:10.1073/pnas.1915070117

33. Nicolas A, Ferrero EE, Martens K, Barrat JL. Deformation and flow of amorphous solids: insights from elastoplastic models. *Rev Mod Phys* (2018) 90:045006. doi:10.1103/revmodphys.90.045006

34. Lin J, Lerner E, Rosso A, Wyart M. Scaling description of the yielding transition in soft amorphous solids at zero temperature. *Proc Natl Acad Sci USA* (2014) 111:14382–7. doi:10.1073/pnas.1406391111

35. Dubey AK, Hentschel HGE, Procaccia I, Singh M. Statistics of plastic events in post-yield strain-controlled amorphous solids. *Phys Rev B* (2016) 93:224204. doi:10.1103/physrevb.93.224204

36. White RA, Dahmen KA. Driving rate effects on crackling noise. *Phys Rev Lett* (2003) 91:085702. doi:10.1103/physrevlett.91.085702

37. Behringer RP, Bi D, Chakraborty B, Henkes S, Hartley RR. *Phys Rev Lett* (2008) 101:268301. doi:10.1103/physrevlett.101.268301

38. Lootens D, VanDamme H, Hébraud P. Giant stress fluctuations at the jamming transition. *Phys Rev Lett* (2003) 90:178301. doi:10.1103/physrevlett.90.178301

39. Liu C, Ferrero EE, Puosi F, Barrat JL, Martens K. Driving rate dependence of avalanche statistics and shapes at the yielding transition. *Phys Rev Lett* (2016) 116:065501. doi:10.1103/physrevlett.116.065501

40. Khfifi M, Loulidi M. Scaling properties of a rice-pile model: inertia and friction effects. *Phys Rev E* (2008) 78:051117. doi:10.1103/physreve.78.051117

41. Salerno KM, Maloney CE, Robbins MO. *Phys Rev Lett* (2012) 109:105703. doi:10.1103/physrevlett.109.105703

42. Salerno KM, Robbins MO. Effect of inertia on sheared disordered solids: critical scaling of avalanches in two and three dimensions. *Phys Rev E* (2013) 88:062206. doi:10.1103/physreve.88.062206

43. Karimi K, Ferrero EE, Barrat JL. Inertia and universality of avalanche statistics: the case of slowly deformed amorphous solids. *Phys Rev E* (2017) 95:013003. doi:10.1103/physreve.95.013003

44. Barés J, Wang D, Wang D, Bertrand T, O'Hern CS, Behringer RP. Local and global avalanches in a two-dimensional sheared granular medium. *Phys Rev E* (2017) 96:052902. doi:10.1103/physreve.96.052902

45. Saitoh K. The role of friction in statistics and scaling laws of avalanches. *Eur Phys J E* (2021) 44:85. doi:10.1140/epje/s10189-021-00089-8

46. Peña AA, McNamara S, Lind PG, Herrmann HJ. Avalanches in anisotropic sheared granular media. *Granular Matter* (2009) 11:243–52. doi:10.1007/s10035-009-0136-4

47. Murphy KA, Dahmen KA, Jaeger HM. Transforming mesoscale granular plasticity through particle shape. *Phys Rev X* (2019) 9:011014. doi:10.1103/physrevx.9.011014

48. Irani E, Chaudhuri P, Heussinger C. Impact of attractive interactions on the rheology of dense athermal particles. *Phys Rev Lett* (2014) 112:188303. doi:10.1103/physrevlett.112.188303

49. Irani E, Chaudhuri P, Heussinger C. Athermal rheology of weakly attractive soft particles. *Phys Rev E* (2016) 94:052608. doi:10.1103/physreve.94.052608

50. Irani E, Chaudhuri P, Heussinger C. Discontinuous shear-thinning in adhesive dispersions. *Phys Rev Fluids* (2019) 4:074307. doi:10.1103/physrevfluids.4.074307

51. Chaudhuri P, Berthier L, Bocquet L. Inhomogeneous shear flows in soft jammed materials with tunable attractive forces. *Phys Rev E* (2012) 85:021503. doi:10.1103/physreve.85.021503

52. Zheng W, Liu H, Xu N. Shear-induced solidification of athermal systems with weak attraction. *Phys Rev E* (2016) 94:062608. doi:10.1103/physreve.94.062608

53. Koeze DJ, Tighe BP. Sticky matters: jamming and rigid cluster statistics with attractive particle interactions. *Phys Rev Lett* (2018) 121:188002. doi:10.1103/physrevlett.121.188002

54. Koeze DJ, Hong L, Kumar A, Tighe BP. Elasticity of jammed packings of sticky disks. *Phys Rev Res* (2020) 2:032047. doi:10.1103/physrevresearch.2.032047

55. Lois G, Blawzdziewicz J, O'Hern CS. Jamming transition and new percolation universality classes in particulate systems with attraction. *Phys Rev Lett* (2008) 100:028001. doi:10.1103/physrevlett.100.028001

56. Herrera-Valencia EE, Sánchez-Villavicencio ML, Soriano-Correa C, Bautista O, Ramírez-Torres LA, Hernández-Abad VJ, et al. Study of the electroosmotic flow of a structured fluid with a new generalized rheological model. *Rheol Acta* (2024) 63:3–32. doi:10.1007/s00397-023-01418-8

57. Luding S. Anisotropy in cohesive, frictional granular media. *J Phys Condens Matter* (2005) 17:S2623–40. doi:10.1088/0953-8984/17/24/017

58. van Hecke M. Jamming of soft particles: geometry, mechanics, scaling and isostaticity. *J Phys Condens Matter* (2010) 22:033101. doi:10.1088/0953-8984/22/3/033101

59. O'Hern CS, Silbert LE, Liu AJ, Nagel SR. Jamming at zero temperature and zero applied stress: the epitome of disorder. *Phys Rev E* (2003) 68:011306. doi:10.1103/physreve.68.011306

60. Radjai F, Roux S. Turbulentlike fluctuations in quasistatic flow of granular media. *Phys Rev Lett* (2002) 89:064302. doi:10.1103/physrevlett.89.064302

61. Mizuno H, Hachiya M, Ikeda A. Structural, mechanical, and vibrational properties of particulate physical gels. *J Chem Phys* (2021) 155:234502. doi:10.1063/5.0072863

62. Mizuno H, Hachiya M, Ikeda A. Phonon transport properties of particulate physical gels. *J Chem Phys* (2022) 156:204505. doi:10.1063/5.0090233

63. Born M, Huang K. *Dynamical theory of crystal lattices*. Oxford: Clarendon Press (1988).

64. MiDi GDR. On dense granular flows. *Eur Phys J E* (2004) 14:341–65. doi:10.1140/epje/i2003-10153-0

65. da Cruz F, Emam S, Prochnow M, Roux JN, Chevoir F. Rheophysics of dense granular materials: discrete simulation of plane shear flows. *Phys Rev E* (2005) 72:021309. doi:10.1103/physreve.72.021309

66. Hatano T. Power-law friction in closely packed granular materials. *Phys Rev E* (2007) 75:060301. doi:10.1103/physreve.75.060301

67. Azéma E, Radjaï F. Internal structure of inertial granular flows. *Phys Rev Lett* (2014) 112:078001. doi:10.1103/PhysRevLett.112.078001

68. Rognon PG, Roux JN, Naaïm M, Chevoir F. Dense flows of cohesive granular materials. *J Fluid Mech* (2008) 596:21–47. doi:10.1017/s0022112007009329

69. Singh A, Magnanimo V, Saitoh K, Luding S. Effect of cohesion on shear banding in quasistatic granular materials. *Phys Rev E* (2014) 90:022202. doi:10.1103/physreve.90.022202

70. Olsson P, Teitel S. Herschel-bulkley shearing rheology near the athermal jamming transition. *Phys Rev Lett* (2012) 109:108001. doi:10.1103/physrevlett.109.108001

71. Andreotti B, Barrat JL, Heussinger C. Shear flow of non-brownian suspensions close to jamming. *Phys Rev Lett* (2012) 109:105901. doi:10.1103/physrevlett.109.105901

72. Vågberg D, Olsson P, Teitel S. Universality of jamming criticality in overdamped shear-driven frictionless disks. *Phys Rev Lett* (2014) 113:148002. doi:10.1103/physrevlett.113.148002

73. Kawasaki T, Coslovich D, Ikeda A, Berthier L. Diverging viscosity and soft granular rheology in non-Brownian suspensions. *Phys Rev E* (2015) 91:012203. doi:10.1103/physreve.91.012203

74. Olsson P. Dimensionality and viscosity exponent in shear-driven jamming. *Phys Rev Lett* (2019) 122:108003. doi:10.1103/physrevlett.122.108003

75. Lerner E, Procaccia I. Locality and nonlocality in elastoplastic responses of amorphous solids. *Phys Rev E* (2009) 79:066109. doi:10.1103/physreve.79.066109

76. Karmakar S, Lerner E, Procaccia I. Statistical physics of the yielding transition in amorphous solids. *Phys Rev E* (2010) 82:055103. doi:10.1103/physreve.82.055103

77. Hentschel HGE, Karmakar S, Lerner E, Procaccia I. Size of plastic events in strained amorphous solids at finite temperatures. *Phys Rev Lett* (2010) 104:025501. doi:10.1103/physrevlett.104.025501

78. Karmakar S, Lerner E, Procaccia I, Zylberg J. Statistical physics of elastoplastic steady states in amorphous solids: finite temperatures and strain rates. *Phys Rev E* (2010) 82:031301. doi:10.1103/physreve.82.031301

79. Dasgupta R, Karmakar S, Procaccia I. Universality of the plastic instability in strained amorphous solids. *Phys Rev Lett* (2012) 108:075701. doi:10.1103/physrevlett.108.075701

80. Talamali M, Petäjä V, Vandembroucq D, Roux S. Avalanches, precursors, and finite-size fluctuations in a mesoscopic model of amorphous plasticity. *Phys Rev E* (2011) 84:016115. doi:10.1103/physreve.84.016115

81. Saitoh K, Mizuno H. Anomalous energy cascades in dense granular materials yielding under simple shear deformations. *Soft Matter* (2016) 12:1360–7. doi:10.1039/c5sm02760h

82. Saitoh K, Mizuno H. Exstrophy cascades in two-dimensional dense granular flows. *Phys Rev E* (2016) 94:022908. doi:10.1103/physreve.94.022908

83. Saitoh K, Mizuno H. Anisotropic decay of the energy spectrum in two-dimensional dense granular flows. *Phys Rev E* (2017) 96:012903. doi:10.1103/physreve.96.012903

84. Mizuno H, Saitoh K, Silbert LE. Elastic moduli and vibrational modes in jammed particulate packings. *Phys Rev E* (2016) 93:062905. doi:10.1103/physreve.93.062905

85. Saitoh K, Magnanimo V, Luding S. A Master equation for the probability distribution functions of forces in soft particle packings. *Soft Matter* (2015) 11:1253–8. doi:10.1039/c4sm02452d

86. Saitoh K, Oyama N, Ogushi F, Luding S. Transition rates for slip-avalanches in soft athermal disks under quasi-static simple shear deformations. *Soft Matter* (2019) 15:3487–92. doi:10.1039/c8sm01966e

87. Cao P, Dahmen KA, Kushima A, Wright WJ, Park HS, Short MP, et al. Nanomechanics of slip avalanches in amorphous plasticity. *J Mech Phys Sol* (2018) 114:158–71. doi:10.1016/j.jmps.2018.02.012